Supporting Information

Orbital Trap of Xenon: Driving Force Distinguishing between Xe and Kr Found at a Single Ag(I) Site in MFI Zeolite at Room Temperature

Akira Oda,[a,b]* Hiroe Kouzai,[c] Kyoichi Sawabe,[a,b] Atsushi Satsuma,[a,b] Takahiro Ohkubo,[c] Kazuma Gotoh,[b,c] Yasushige Kuroda[c]*

[a] Department of Materials Chemistry, Graduate School of Engineering, Nagoya University, Furo-cho, Chikusa-ku, Nagoya 464-8603, Japan.

[b] Elements Strategy Initiative for Catalysts and Batteries (ESICB), Kyoto University, Kyoto 615-8520, Japan.

[c] Department of Chemistry, Graduate School of Natural Science and Technology, Okayama University, 3-1-1 Tsushima, Kita-ku, Okayama 700-8530, Japan.

Corresponding Authors

*E-mail: akira@chembio.nagoya-u.ac.jp (A. O.); kuroda@cc.okayama-u.ac.jp (Y. K.)

1. Supporting Discussion.

1.1. Validity of Our Computational Method. Previously, we have reported the chemisorption of Xe on a single Cu(I) site in MFI at 298 K.[1] Based on in situ X-ray absorption fine-structure (XAFS) and differential heat of adsorption of Xe, the Cu(I)−Xe bond length was elucidated to be 2.5 Å and the maximum adsorption energy was about 60 kJ mol^{-1}. Our computational approach applied in the present study was able to reproduce these experimental data characteristic of the Cu(I)−Xe interaction. **Figure S2a** shows the optimized periodic density functional theory (DFT) models representing the Xe adsorption at the single Cu(I) site located at the 10 membered ring (10MR) position. The hybrid DLPNO-CCSD(T):PBE-D3(BJ) adsorption energy was computed as −61.9 kJ mol^{-1}. The obtained value agreed well with the differential heat of adsorption of Xe observed in the adsorption process at 298 K in the low-pressure region. The AIMD simulation visualized the dynamic positions of the Cu and Xe atoms, demonstrating the localization of the Cu−Xe adduct at the intersection position (**Figure S2b**). The dynamic distance of Cu(I)−Xe observed within 25 ps AIMD simulation was 2.509±0.083 Å (**Figure S2c**), consistent well with the EXAFS datum, i.e., 2.50±0.02 Å.[1] Considering the good correlation between the experimental and computational data, we can reasonably claim that the validity of our computational approach used here is very high; the Ag−Xe interaction confined within the zeolite cavity would be computed at a high accuracy level.

1.2. Dynamic Coordination Sphere of the Single Ag(I) Site. The trajectories of the dynamic distances between the Ag and the lattice oxygens or the framework Al atom in the 10MR and 6MR sites at 300 K were depicted in **Figures S8,** where the lattice oxygens of interest were labeled as $1O_{Al,Si}$, $2O_{Al,Si}$, $1O_{Si,Si}$, and $2O_{Si,Si}$; see the schemes in the figures. At the 10MR position, the Ag−$1O_{Al,Si}$ and Ag–$2O_{Al,Si}$ bonds were stable; their lengths were almost constant within the 25 ps AIMD simulation. Other lattice oxygens did not form any bond with the single Ag(I) species. Therefore, the two-coordination sphere of Ag(I) was constrained at this site. On the other hand, a complicated dynamic geometry was found at the 6MR site. The Ag−$1O_{Al,Si}$ and Ag−$2O_{Al,Si}$ bonds were stable, as the 10MR position, but the wave-like trajectories of the dynamic distances of Ag−$1O_{Si,Si}$ and Ag−$2O_{Si,Si}$ were observed. When the dynamic Ag−$1O_{Si,Si}$ distance becomes shortened, the dynamic Ag−$2O_{Si,Si}$ distance becomes longer. Inversely, when the dynamic Ag−$1O_{Si,Si}$ distance becomes longer, the dynamic Ag−$2O_{Si,Si}$ becomes short. These coordination dynamics indicate the isomerization of the T-shape structure of the Ag(I)−$(O_{Al,Si})_2(O_{Si,Si})_1$ as shown in the scheme in **Figure S8b**. Accordingly, the 6MR site constrains the three-coordination sphere of Ag(I).

1.3. Dynamic Coordination Sphere of the Ag_n^{m+} Cluster Sites. As evidenced from in situ XAFS data, the present Ag/MFI sample contains the silver clusters as the minor spectator sites. The EXAFS fitting analyses provided the coordination number of silver atoms present in a first shell region of 0.7±0.4, suggesting the formation of the small silver clusters, i.e. dimer, trimer, and tetramer. In our previous works, the plausible models of the silver cluster sites were systematically explored using the DFT cluster calculations at B3PW91/SDD, 6-31G(d), 3-21G level.[2-3] The local minima of Ag dimer, trimer, and tetramer were found on the single or dual

framework AlO_4 sites. The Ag dimer was stabilized only at the single framework AlO_4 tetrahedra site.[2] On the other hand, the Ag trimer and tetramer were formed on both the single and nearest AlO_4 tetrahedra sites.[2-3]

Taking accounts of the previous computational results, as well as the EXAFS data collected in the present study, the periodic DFT model of the Ag_n^{m+} cluster sites were constructed (**Figure S11, left and middle**). Consistently with the DFT cluster models reported in our previous works,[2-3] reasonable models were obtained. The optimized Ag_2^+ cluster model featured the linear Ag−Ag motif where one of the Ag ions interacts with two oxygens of the AlO_4 tetrahedra site (**Figure S11a, left and middle**). The optimized Ag_3^+ and Ag_3^{2+} cluster models featured the triangular motifs with the slightly broken C_{2v} symmetry (**Figures S11b and c, left and middle**). The optimized Ag_4^+ and Ag_4^{2+} cluster models featured the butterfly or tetrahedra shapes (**Figures S11d and e, left and middle**). AIMD simulation demonstrated that these structures are stable at 300 K (**Figure S11, right**). The simulated dynamic Ag–Ag bond lengths were in a range of 2.6−2.8 Å (**Table S1**), in a harmony with the best-fit EXAFS parameters (**Table 1**).

1.4. Xe Adsorption Property of the Ag_n^{m+} Cluster Sites. The Xe adsorption properties of the Ag_n^{m+} cluster sites were computationally investigated using the periodic DFT models of the Ag_n^{m+} cluster sites. The Xe atom was placed in the vicinities of the Ag_n^{m+} cluster sites and optimized at 0 K (**Figure S12, left and middle**). The Ag−Xe distances, as well as the Ag−Ag distances were summarized in **Table S1**. Apparently, the Ag−Xe distances observed at Ag_n^{m+} cluster sites were longer than that for the single Ag(I) site.

The dynamic Ag−Xe distances were found to be *site-dependent* (**Figure S12, right)**. The short Ag−Xe distances were observed only at the Ag_3^{2+} and Ag_4^{2+} clusters: ca. 3.3 Å. Other Ag_n^+ clusters loosely interacted with Xe, as evidenced by the longer Ag−Xe distance trajectories with the large fluctuations. The Ag−Xe distance of shorter than 3 Å was not observed in all the cases except for the single Ag(I) site; it was only the single Ag(I) site that forms the short Ag(I)−Xe bond (**Figure S13**).

1.5. Importance of atomicity of the Silver Ion-Exchanged Sites toward Xe Fixation. The acidity imparted by the zeolite framework was most pronounced on the single Ag(I) state; σ-contributions were significantly small for the Ag−Xe interactions over the Ag_n^{m+} cluster stabilized on the framework AlO_4 tetrahedra. **Figure S14** shows the electron density differences upon the Xe addition to Ag_n^{m+} cluster sites. For comparison, the result for the single Ag(I) site was also depicted. Apparently, the stable σ-bond was formed only on the single Ag(I) site. Slightly, the σ-bond was found on the $[Ag_3Xe]^{2+}$ and $[Ag_4Xe]^{2+}$ cluster models, but their contributions are significantly small. Other $[Ag_nXe]^+$ clusters show no covalent Ag−Xe bond. The changes in LUMO for the Ag_n^{m+} cluster upon the Xe binding were not so enormous (**Figures S15**; also refer to **Figure S16** for understanding of the LUMOs). Consistently, all the Ag_n^{m+} clusters showed poor Xe adsorption properties; the dynamic Ag−Xe distances were longer than 3.27 Å with the large fluctuations (**Figures S12 and S13**). Apparently, the Ag_n^{m+} clusters are not effective toward Xe fixation by comparison with the single Ag(I) site. How could the cluster-size dependency happen? It can be explained by considering that the addition of electron-rich silver atoms to the ion-exchanged silver cation leads to the reduction of the electron-accepting nature

essential for the Xe fixation. Accordingly, the Xe adsorption/separation properties found in the present study do originate from the superior electron-accepting nature of the single silver ion endowed by the zeolite lattice ligation, simultaneously supporting the single Ag(I) site model.

1.6. Effect of the residual water on the adsorption process. It is well known that zeolites are easy to adsorb water. Since the pre-evacuation temperature is low (473 K), it is expected that our sample contains the residual water species. To evaluate the contribution of the residual water species to the adsorption processes, we performed additional experiments described below.

We first performed IR measurement on the Ag/MFI sample evacuated at 473 K (**Figure S18**). In the region of 4000–3000 cm^{-1}, the IR features attributed to ν_{O-H} of the residual water species were detected; however, its contribution is very small.

Complete dehydration is possible if the metal ion-exchanged zeolites are evacuated at 873 K for 4 h. To evaluate how the residual water species affect the adsorption process, we next measured the CO adsorption isotherms for the Ag/MFI sample evacuated at 473 K and 873 K for 4 hours and compared with each other (**Figure S19**). We can see that these are almost equivalent in a low-pressure region where the CO adsorption occurs at the single Ag(I) site. This indicates that the local geometry and number of the single Ag(I) sites are equivalent for the 473 K and 873 K-evacuated samples; thus, we can reasonably claim that 473 K-evacuation leads to the removal of almost all water molecules from the Ag(I)-zeolite, and the trace amount of water molecule scarcely affect the adsorption process.

2. Supporting Data.

Table S1. Selected structural parameters of the periodic DFT models of $[Ag_n]^{m+}$ and $[Ag_nXe_1]^{m+}$ at 0 K and 300 K.

Site	Bond label	Atomic distance at 0 K (Å)		Dynamic distance at 300 K (Å)	
		Before Xe adsorption	After Xe adsorption	Before Xe adsorption	After Xe adsorption
Ag_1^+	Ag−Xe	–	2.755	–	2.806±0.139
$Ag_2^{+\bullet}$	Ag1−Ag2	2.711	2.702	2.711±0.090	2.716±0.114
	Ag1−Xe	–	3.695	–	5.733±1.621
	Ag2−Xe	–	3.342	–	6.021±1.605
Ag_3^+	Ag1−Ag2	2.662	2.665	2.685±0.090	2.692±0.109
	Ag1−Ag3	2.640	2.637	2.669±0.084	2.680±0.092
	Ag2−Ag3	2.621	2.617	2.644±0.082	2.662±0.098
	Ag1−Xe	–	4.094	–	5.572±1.573
	Ag2−Xe	–	4.205	–	6.291±1.778
	Ag3−Xe	–	4.306	–	7.481±1.606
$Ag_3^{2+\bullet}$	Ag1−Ag2	2.866	2.830	2.812±0.122	2.816±0.144
	Ag1−Ag3	2.738	2.724	2.780±0.122	2.865±0.316
	Ag2−Ag3	2.799	2.810	2.769±0.105	2.812±0.146
	Ag1−Xe	–	3.768	–	3.271±0.439
	Ag2−Xe	–	4.311	–	4.228±0.686
	Ag3−Xe	–	3.101	–	4.972±0.843
$Ag_4^{+\bullet}$	Ag1−Ag2	2.696	2.694	[a]2.846±0.488	2.712±0.105
	Ag1−Ag3	2.710	2.716	[a]2.729±0.121	2.739±0.114
	Ag1−Ag4	2.760	2.757	[a]2.777±0.195	2.788±0.124
	Ag2−Ag3	2.719	2.722	[a]2.862±0.390	2.750±0.119
	Ag2−Ag4	2.689	2.707	[a]4.126±0.752	2.743±0.171
	Ag3−Ag4	4.723	4.733	[a]2.765±0.131	4.619±0.249
	Ag1−Xe	–	4.453	–	6.611±2.257
	Ag2−Xe	–	5.960	–	7.507±1.919
	Ag3−Xe	–	3.563	–	5.736±2.510
	Ag4−Xe	–	7.069	–	8.519±1.772
Ag_4^{2+}	Ag1−Ag2	2.743	2.734	2.769±0.109	2.753±0.110
	Ag1−Ag3	2.783	2.780	2.732±0.103	2.768±0.118
	Ag1−Ag4	2.807	2.797	2.827±0.126	2.794±0.138
	Ag2−Ag3	2.745	2.768	2.777±0.123	2.819±0.152
	Ag2−Ag4	2.790	2.759	2.747±0.137	2.773±0.139
	Ag3−Ag4	2.719	2.730	2.762±0.109	2.759±0.118
	Ag1−Xe	–	4.281	–	4.540±0.524
	Ag2−Xe	–	4.875	–	5.010±0.778
	Ag3−Xe	–	3.305	–	3.319±0.471
	Ag4−Xe	–	5.629	–	5.623±0.457

[a]Only in the AIMD simulation of the Ag_4^+ cluster model at 300 K, an exchange of positions of four silver atoms was observed. Therefore, the structural parameters of the Ag_4^+ at 300 K were different from the structural parameters obtained at 0 K, as well as the Xe adsorption model at 300 K.

Table S2. Ng adsorption energies computed at PBE-D3(BJ) and DLPNO-CCSD(T):PBE-D3(BJ) levels.

Models	E_{ads} (kJ mol^{-1})	
	PBE-D3(BJ)	DLPNO-CCSD(T):PBE-D3(BJ)
Ag_1−Xe at 10MR	−78.5	−53.6
Ag_1−Kr at 10MR	−55.3	−37.7
Ag_1−Xe at 6MR	−63.2	−46.0
Ag_1−Kr at 6MR	−43.3	−32.0

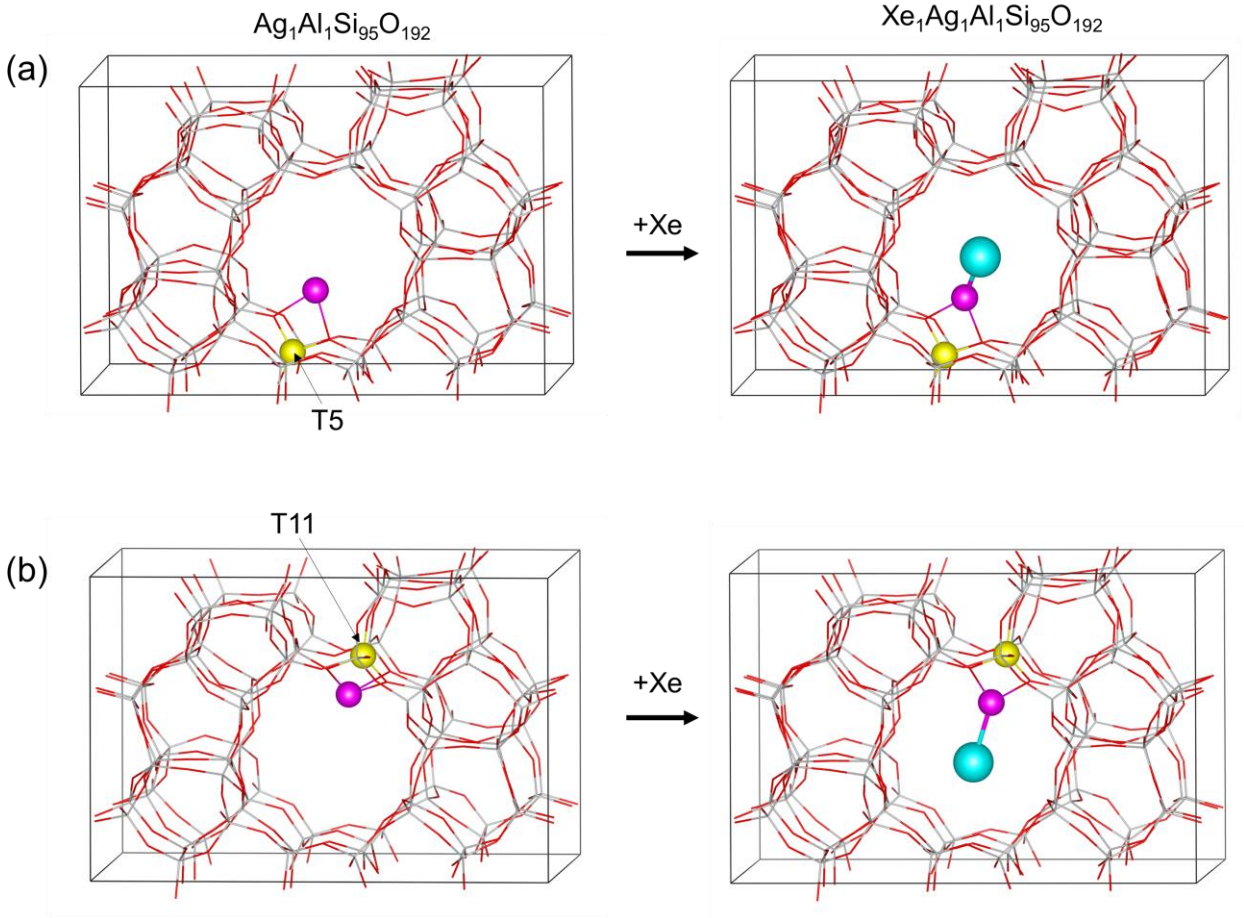

Figure S1. The optimized periodic DFT models of the single Ag(I) and Ag(I)−Xe sites at (a) 10MR and (b) 6MR positions. Legend: pink, Ag; light blue, Xe; gray, Si; yellow, Al; red, O.

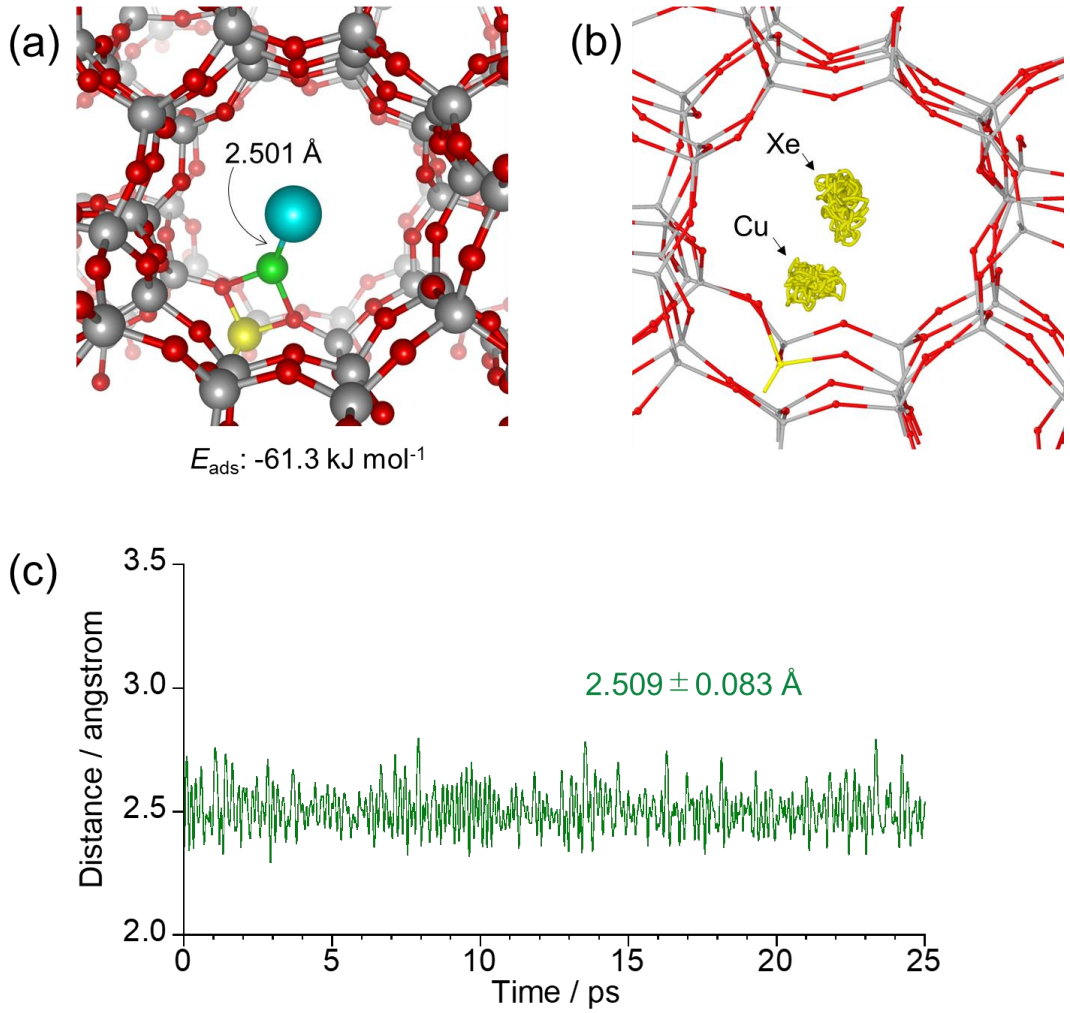

Figure S2. (a) The periodic DFT model of the Cu(I)–Xe adduct in the MFI zeolite cavity, which was optimized at 0 K. (b) Trajectories of the dynamic positions of Cu and Xe atoms within the AIMD simulation at 300 K for 25 ps, which were depicted as yellow solid lines. All the atoms were depicted in wireframe style for clarity. (c) The trajectory of the dynamic Cu(I)−Xe bond length. Legend: green, Cu; light blue, Xe; gray, Si; yellow, Al; red, O.

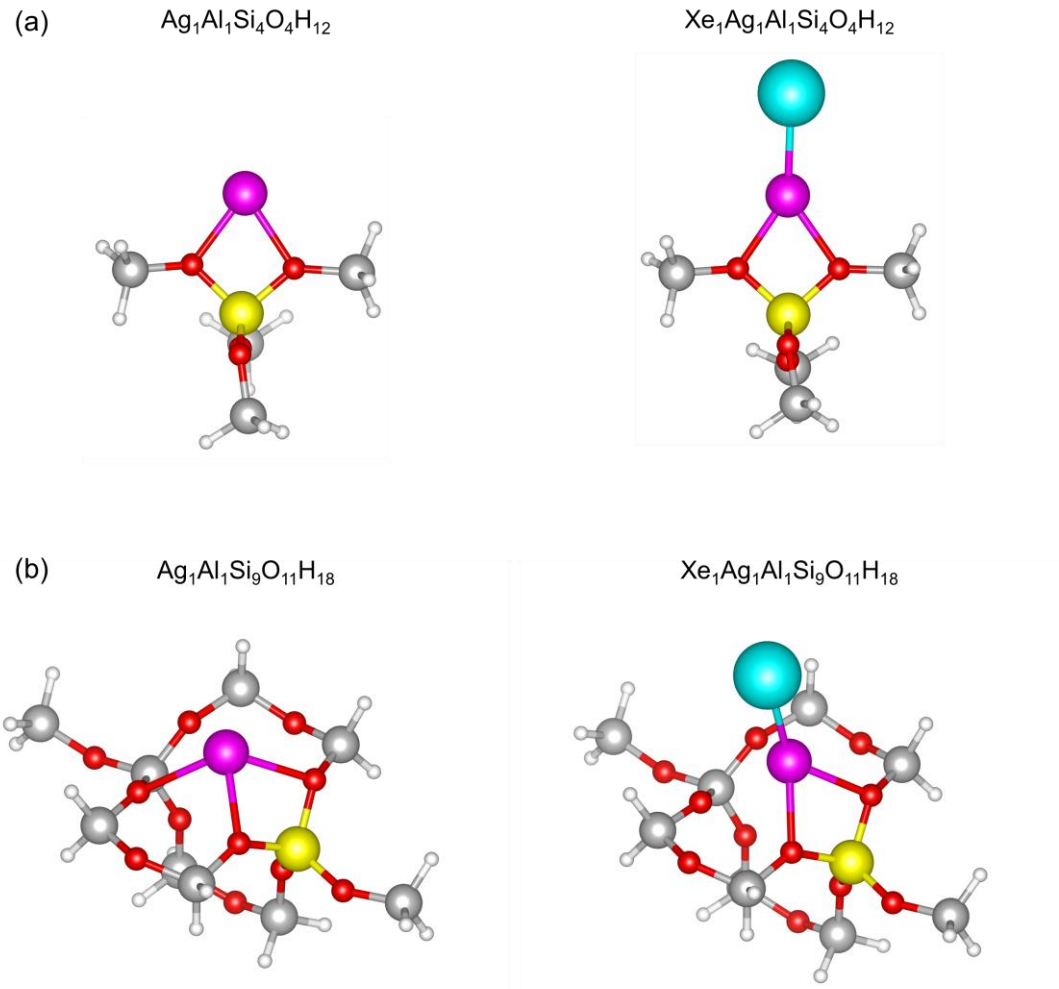

Figure S3. The geometries used for the TD-DFT and ^{129}Xe chemical shift calculations for the Xe adsorption process on the single Ag(I) sites: (a) 10MR models with the formula of $Ag_1Al_1Si_4O_4H_{12}$, and $Xe_1Ag_1Al_1Si_4O_4H_{12}$; (b) 6MR models with the formula of $Ag_1Al_1Si_9O_{11}H_{18}$, and $Xe_1Ag_1Al_1Si_9O_{11}H_{18}$. Legend: pink, Ag; light blue, Xe; gray, Si; yellow, Al; red, O; white, H.

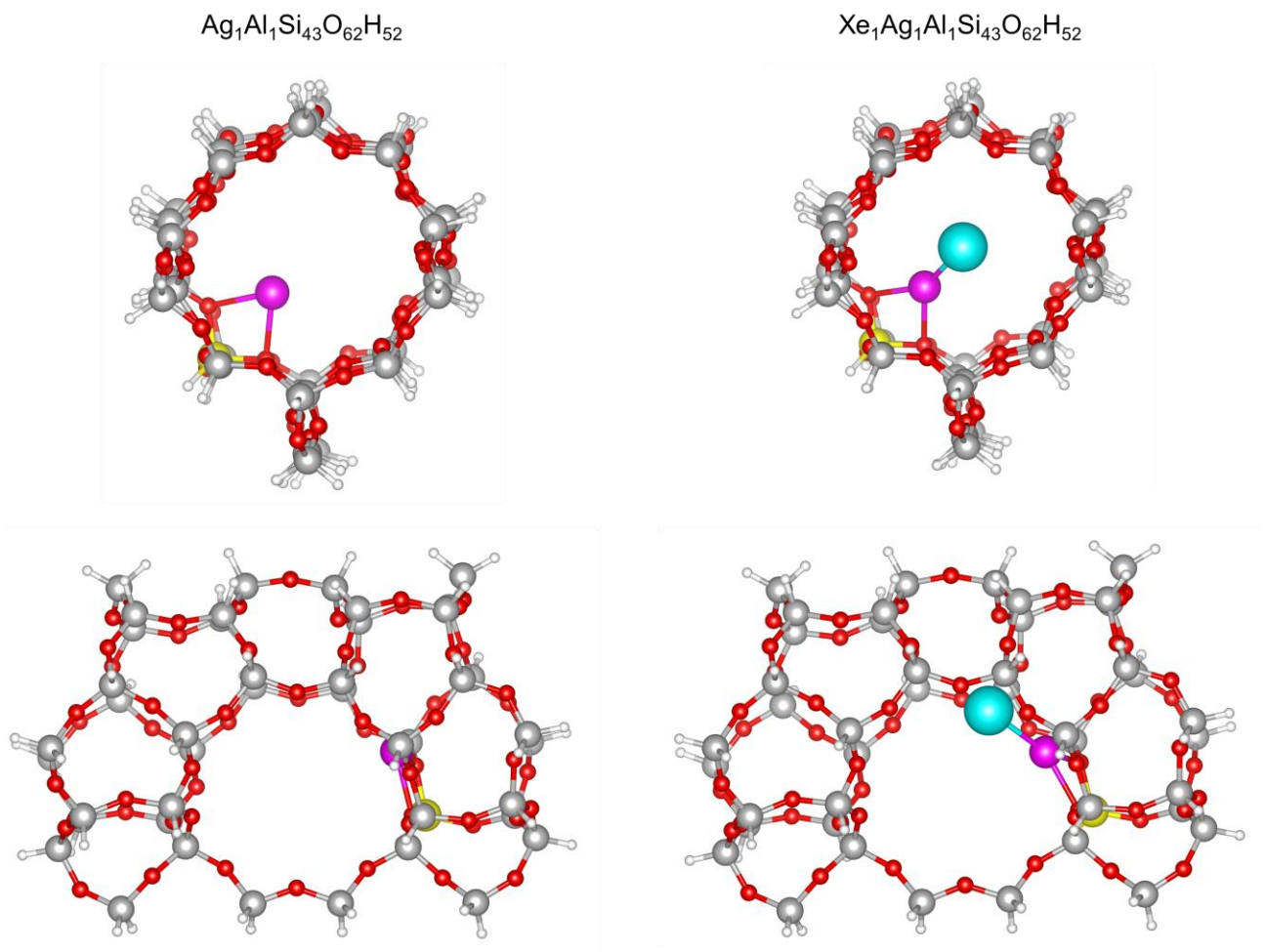

Figure S4. The geometries used for the energy calculation on the Xe adsorption on the single Ag(I) site at 10MR position: $Ag_1Al_1Si_{43}O_{62}H_{52}$ and $Xe_1Ag_1Al_1Si_{43}O_{62}H_{52}$. Legend: pink, Ag; light blue, Xe; gray, Si; yellow, Al; red, O; white, H.

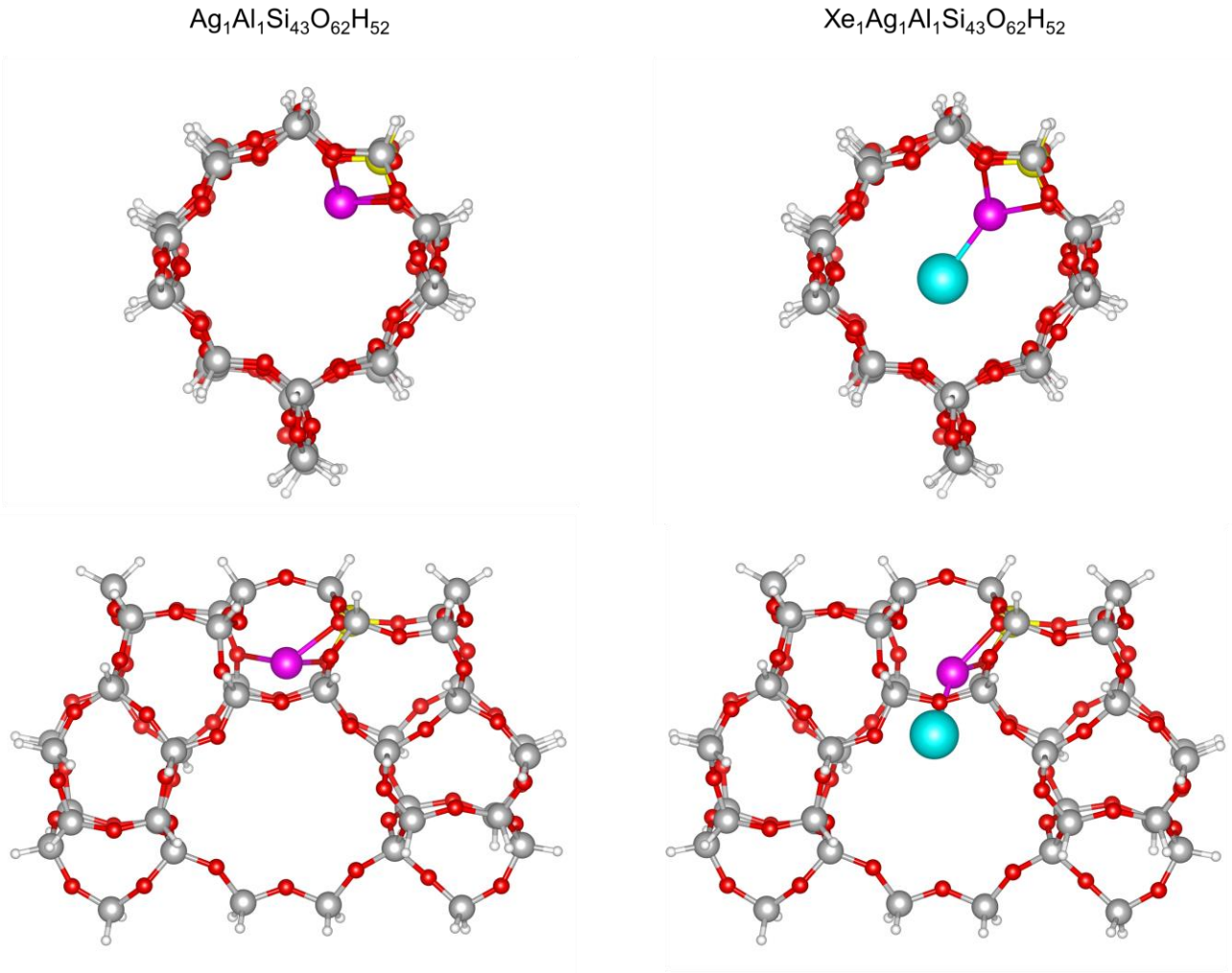

Figure S5. The geometries used for the energy calculation on the Xe adsorption on the single Ag(I) site at 6MR position: $Ag_1Al_1Si_{43}O_{62}H_{52}$, and $Xe_1Ag_1Al_1Si_{43}O_{62}H_{52}$. Legend: pink, Ag; light blue, Xe; gray, Si; yellow, Al; red, O; white, H.

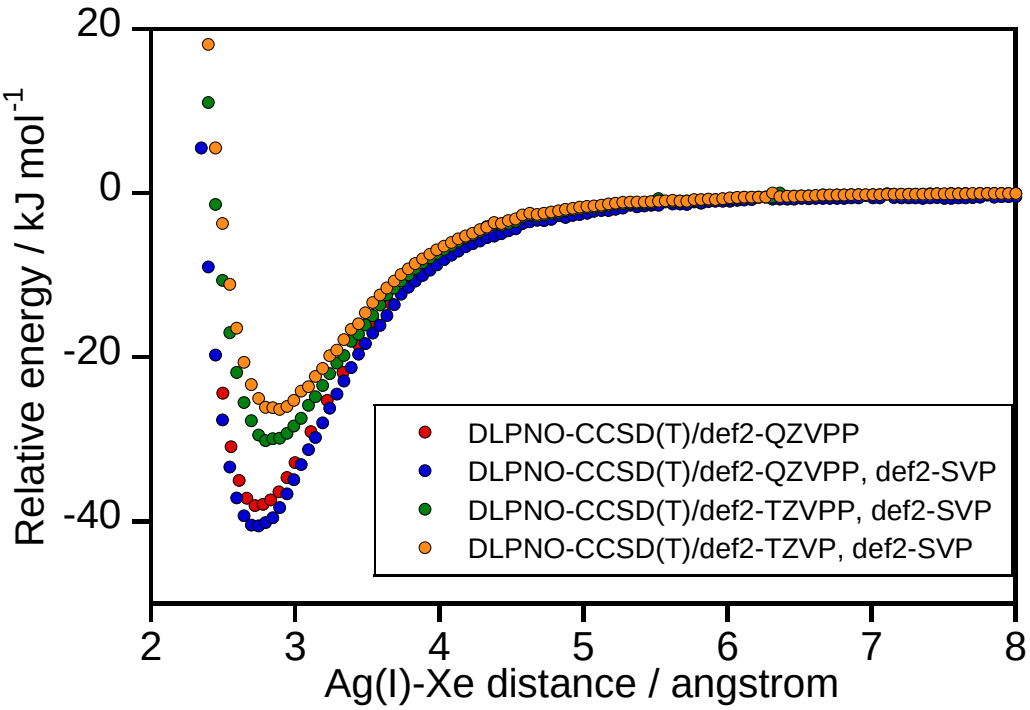

Figure S6. The computational level dependency of the PESs of the Ag(I)−Xe adduct along the Ag(I)−Xe distance. $Xe_1Ag_1Al_1Si_4O_4H_{12}$ geometry shown in **Figure S3a**

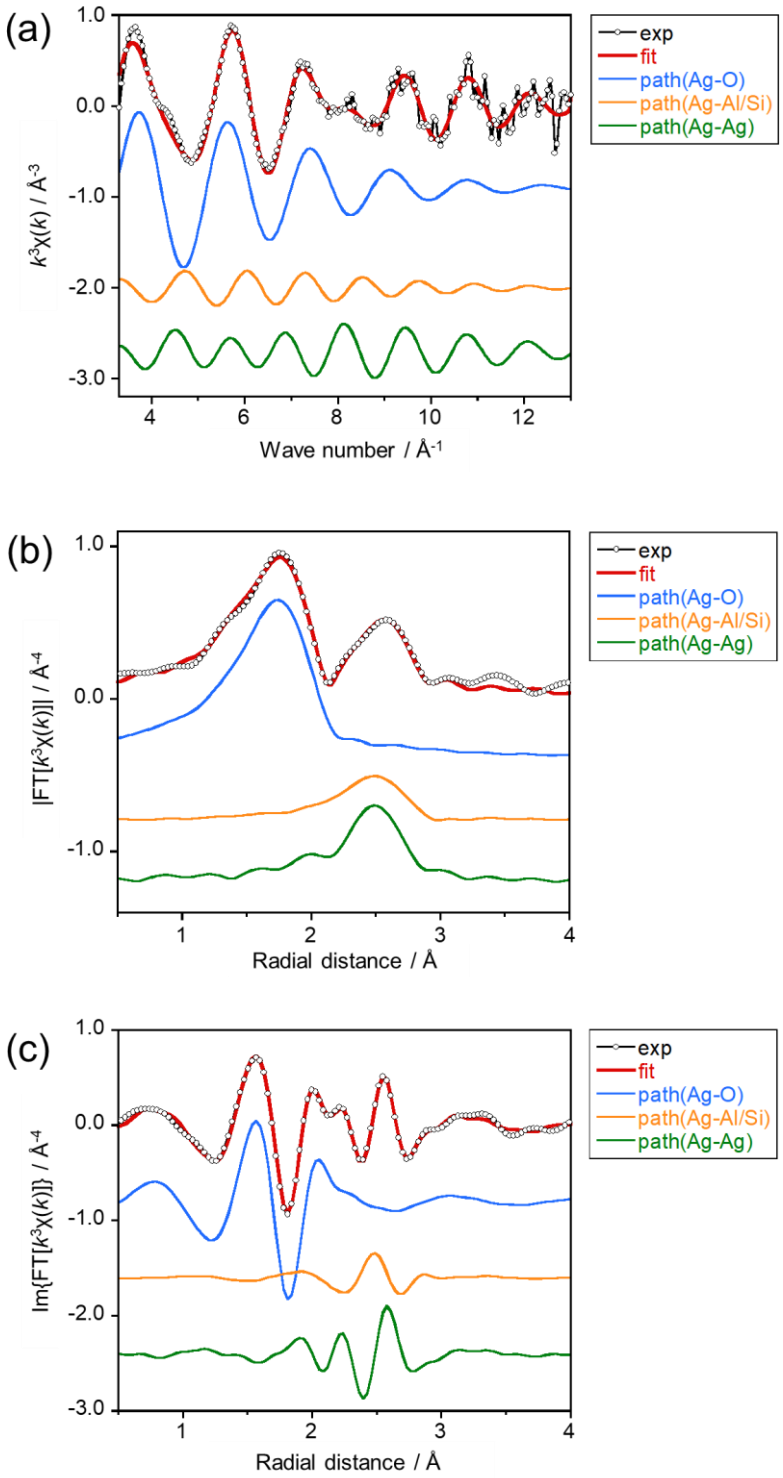

Figure S7. (a) The experimental $k^3\chi(k)$ function (black line) with the best fit function (red line). (b, c) Phase uncorrected *R*-space EXAFS spectra obtained through the Fourier transform of the $k^3\chi(k)$ function in a range of $3.2 < k < 13$ Å^{-1} with the best-fit spectra (red line): (b) modulus; (c) imaginary part. For the EXAFS fitting, a combination of the Ag−O, Ag−Si/Al, and Ag−Ag back scatterings were considered. The respective contributions of the Ag−O, Ag−Si/Al, and Ag−Ag back scatterings were also included in the figures.

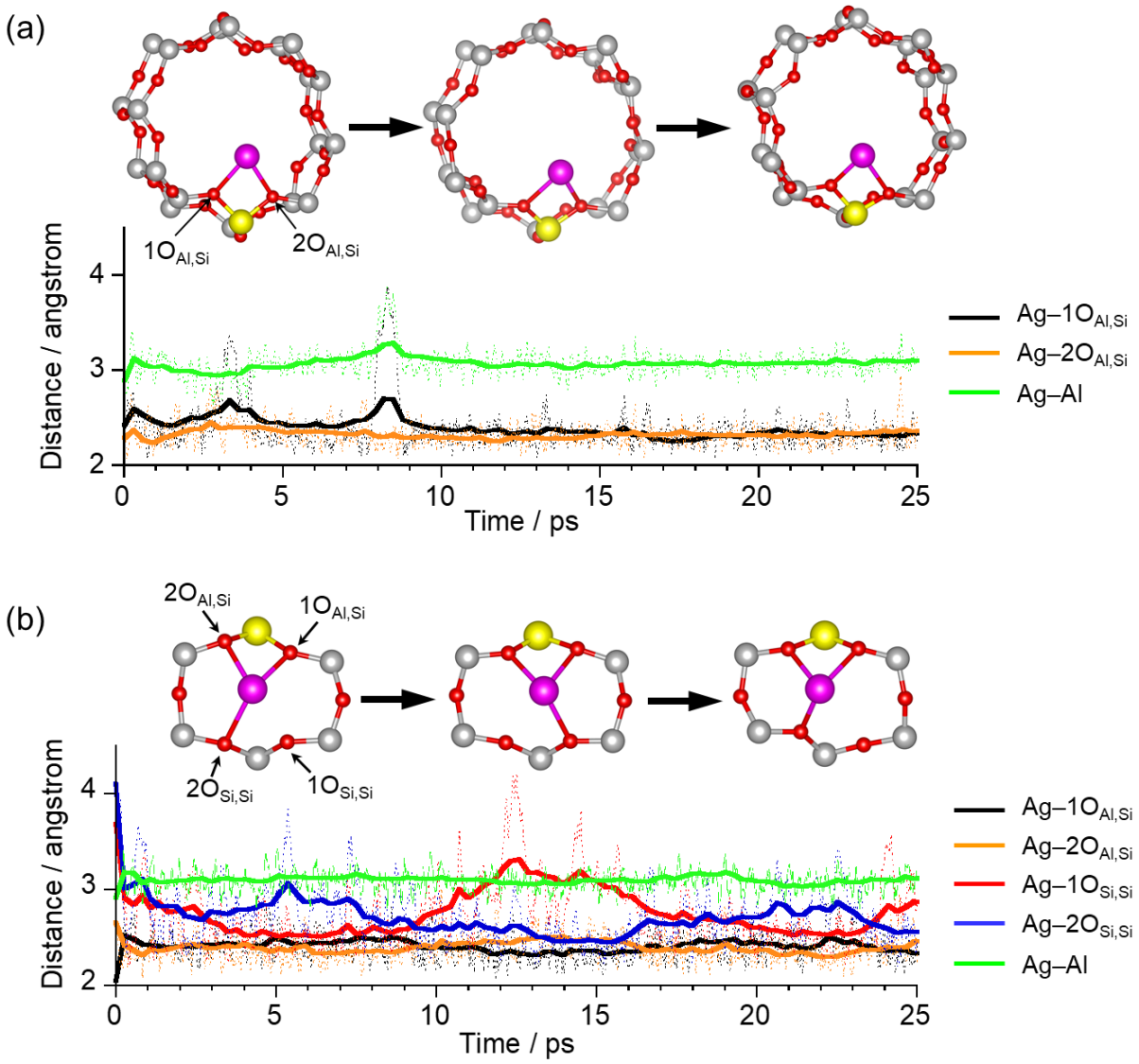

Figure S8. Dynamic Ag–O_L distances observed within the 300 K AIMD simulations for 25 ps using the (a) 10MR and (b) 6MR models. Moving averages were also given as solid lines. Variations of the local structures of the single Ag(I) sites were also schematically depicted. Legend: pink, Ag; gray, Si; yellow, Al; red, O.

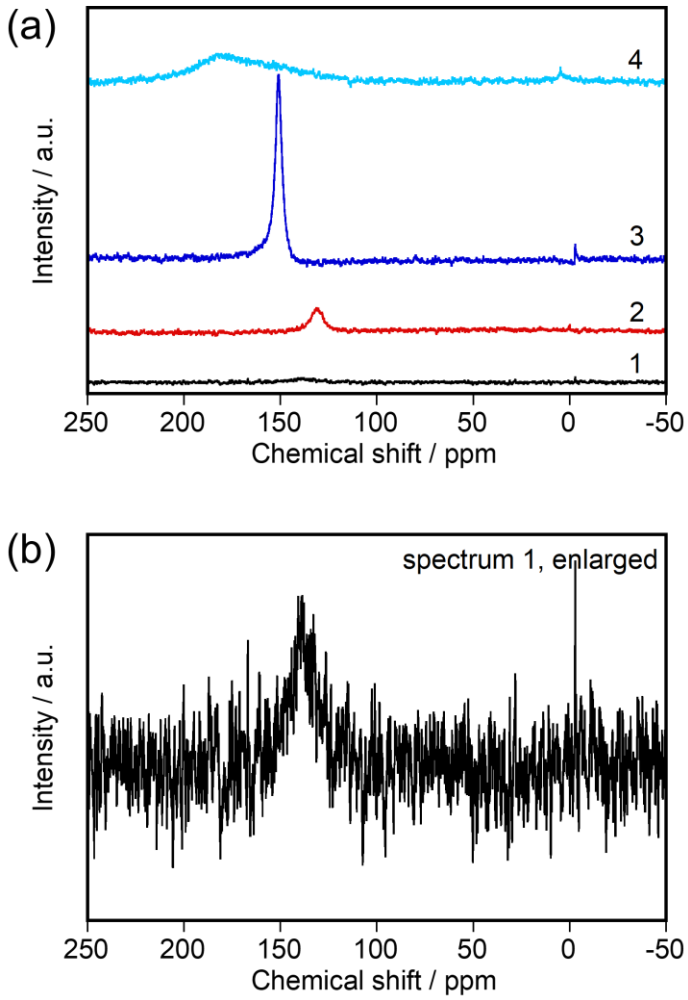

Figure S9. (a) ^{129}Xe NMR spectra of H/MFI sample with different Xe adsorbed amounts: (1) 0.05 mmol g^{-1}, (2) 0.17 mmol g^{-1}, (3) 0.63 mmol g^{-1}, (4) 0.96 mmol g^{-1}. For clarity, the enlarged graph of spectrum 1 was also given in (b).

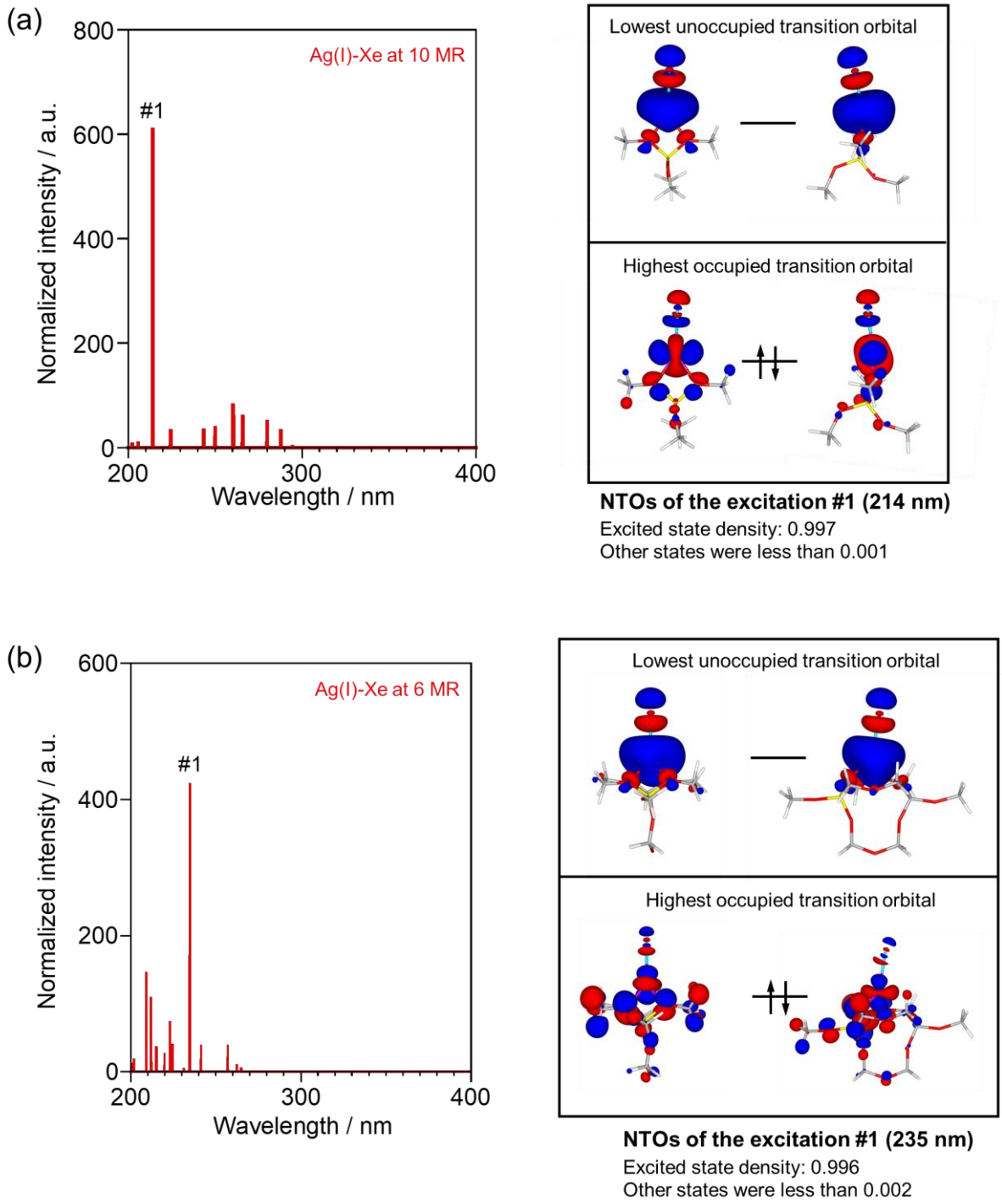

Figure S10. Natural transition orbitals (NTOs) of the Ag(I)-4*d* → σ_{Ag-Xe}* excitations predicted by the TD-DFT calculations: single Ag(I)−Xe site at (a) 10MR and (right) 6MR positions. Legend: pink, Ag; light blue, Xe; gray, Si; yellow, Al; red, O; white, H.

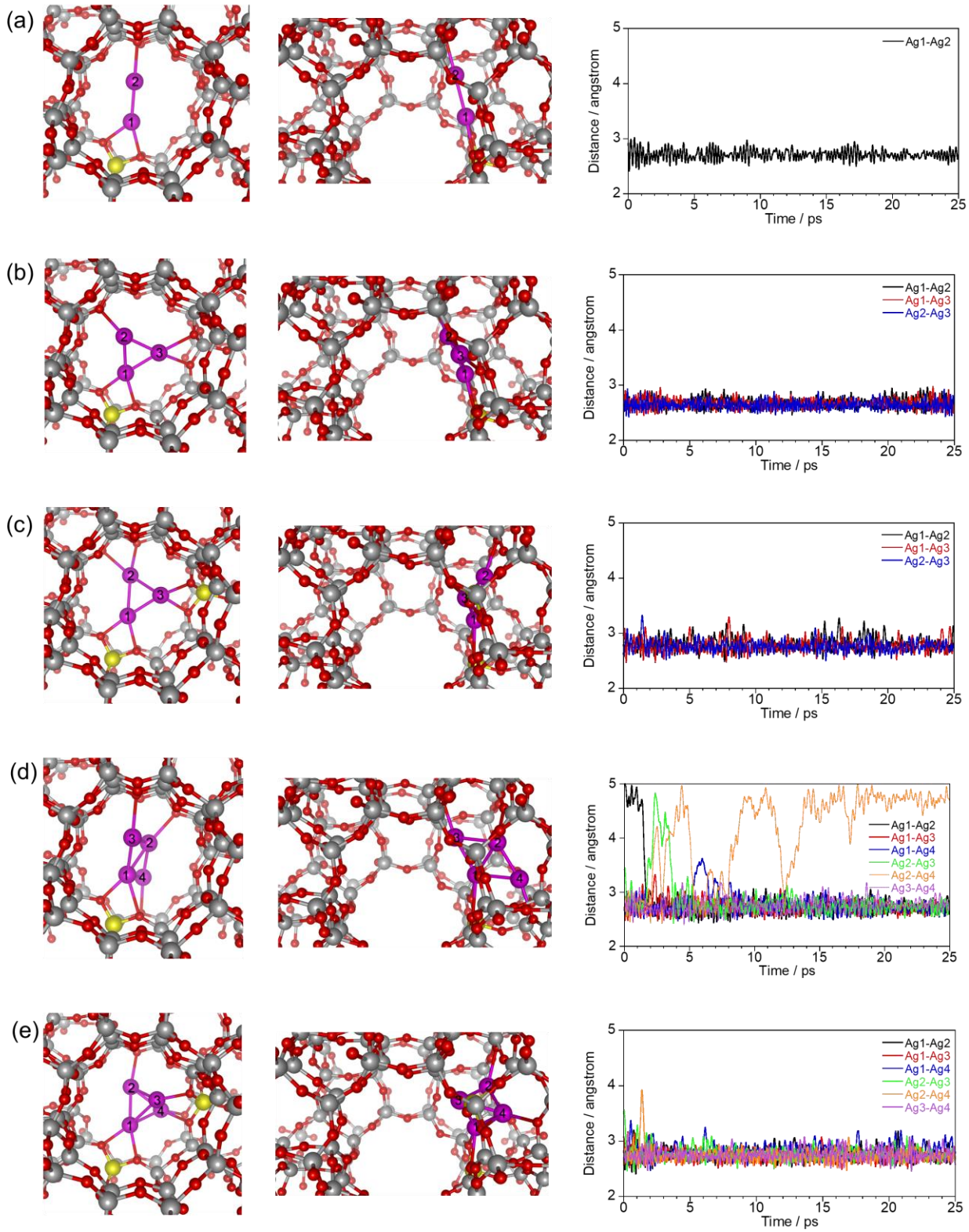

Figure S11. Optimized periodic DFT models of $[Ag_n]^{m+}$: (a) $[Ag_2]^{+\bullet}$; (b) $[Ag_3]^{+}$; (c) $[Ag_3]^{2+\bullet}$; (d) $[Ag_4]^{+\bullet}$; (e) $[Ag_4]^{2+}$. Trajectories of the dynamic Ag−Xe distances observed within AIMD simulation of $[Ag_n]^{m+}$ cluster models at 300 K for 30 ps were also given in the right panel. Legend: pink, Ag; light blue, Xe. Note that only in the AIMD simulation of the Ag_4^+ cluster model at 300 K, an exchange of positions of four silver atoms was observed. Therefore, the dynamic structural parameters of the Ag_4^+ at 300 K were different from the structural parameters obtained at 0 K. Legend: pink, Ag; gray, Si; yellow, Al; red, O.

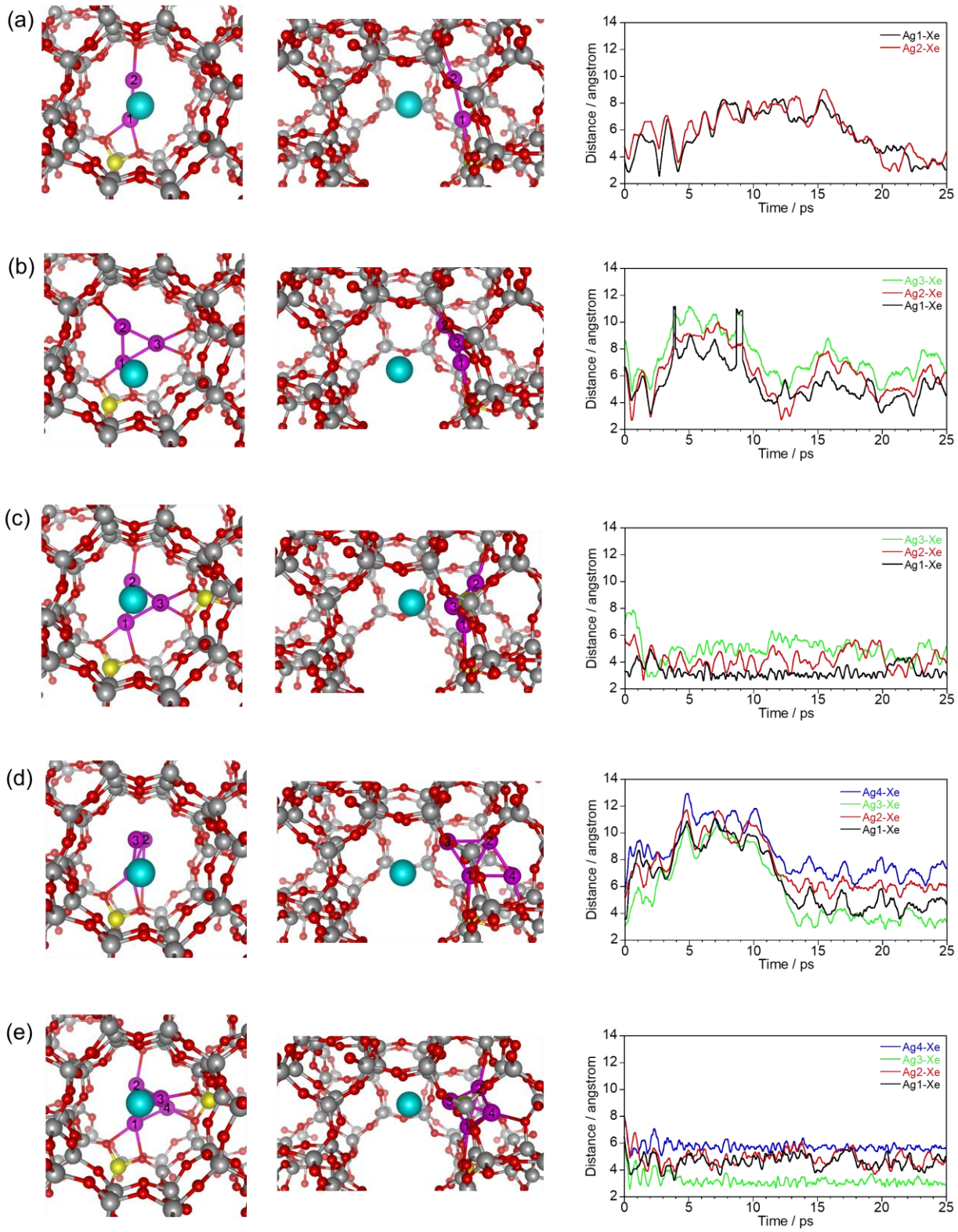

Figure S12. Optimized periodic DFT models of $[Ag_nXe_1]^{m+}$: (a) $[Ag_2Xe_1]^{+\bullet}$; (b) $[Ag_3Xe_1]^{+}$; (c) $[Ag_3Xe_1]^{2+\bullet}$; (d) $[Ag_4Xe_1]^{+\bullet}$; (e) $[Ag_4Xe_1]^{2+}$. Both straight and sinusoidal channel views were shown. In the right panel, AIMD simulated trajectories of the dynamic Ag−Xe distances at 300 K were given. Legend: pink, Ag; light blue, Xe; gray, Si; yellow, Al; red, O.

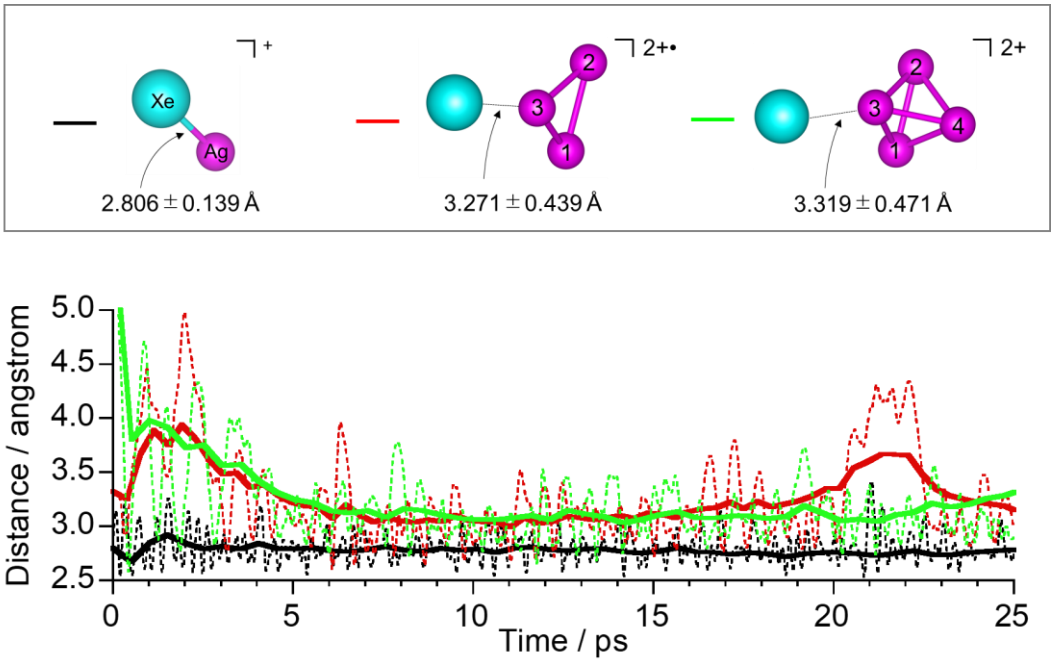

Figure S13. Comparisons of the dynamic Ag–Xe distances observed within AIMD simulations of $[Ag_1Xe_1]^+$, $[Ag_3Xe_1]^{2+\bullet}$, and $[Ag_4Xe_1]^{2+}$ models at 300 K. Moving averages were also given as solid lines. Here, only the shortest Ag−Xe distances observed in the respective sites were depicted. Legend: pink, Ag; light blue, Xe.

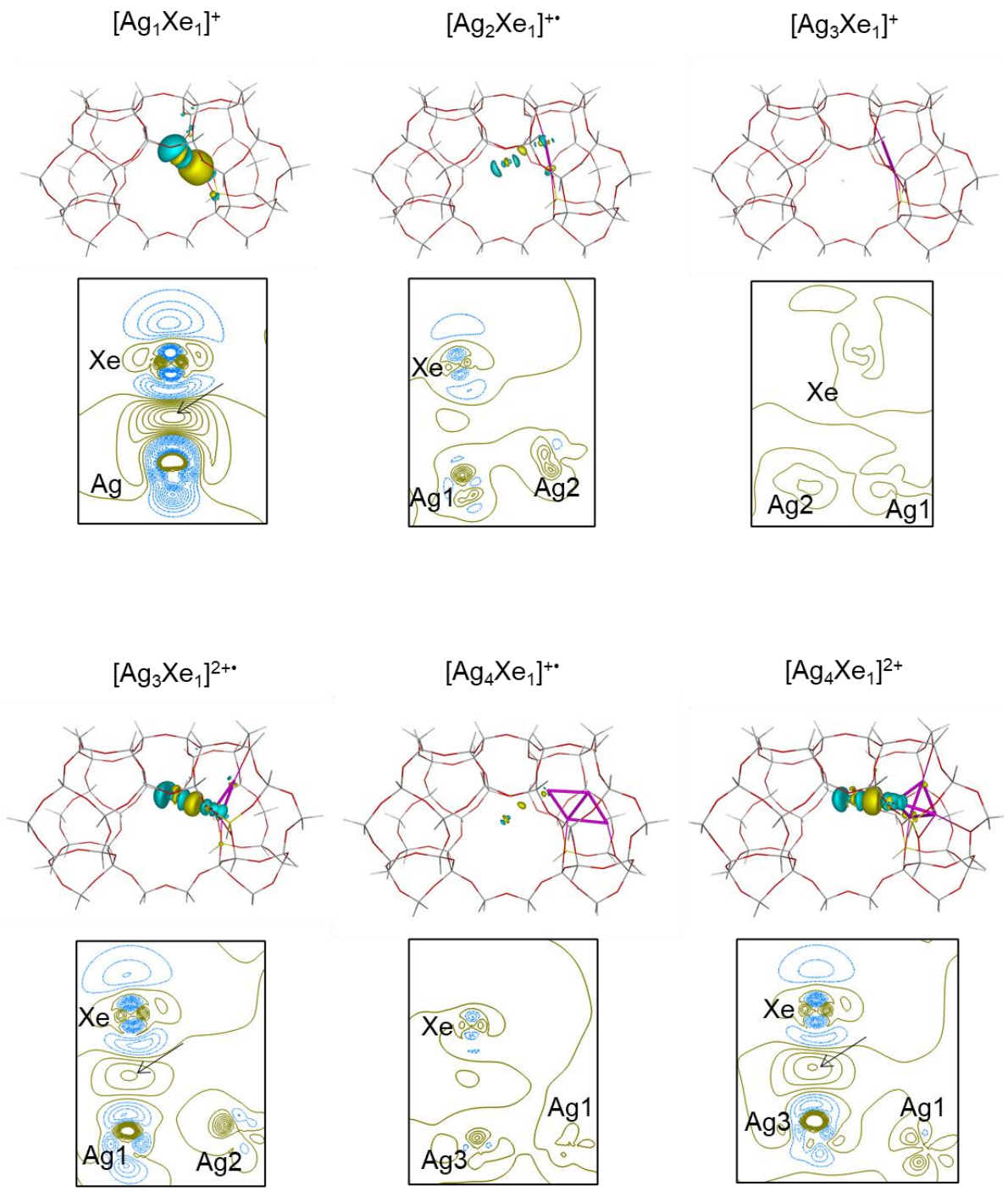

Figure S14. 3D isodensity plots of the SCF-electron density differences between the $[Ag_nXe_1]^{m+}$ cluster and the fragments ($[Ag_n]^{m+}$ and Xe). The yellow and blue surfaces represent charge accumulation and depletion, respectively, which were drawn from −0.01 to +0.01 e/ A^3, with a contour interval of 0.001 e/$Å^3$. For clarity, the geometries were represented as wireframe style. Contour plots of the SCF-electron density differences were also given in bottom. Legend: pink, Ag; light blue, Xe; gray, Si; yellow, Al; red, O; white, H.

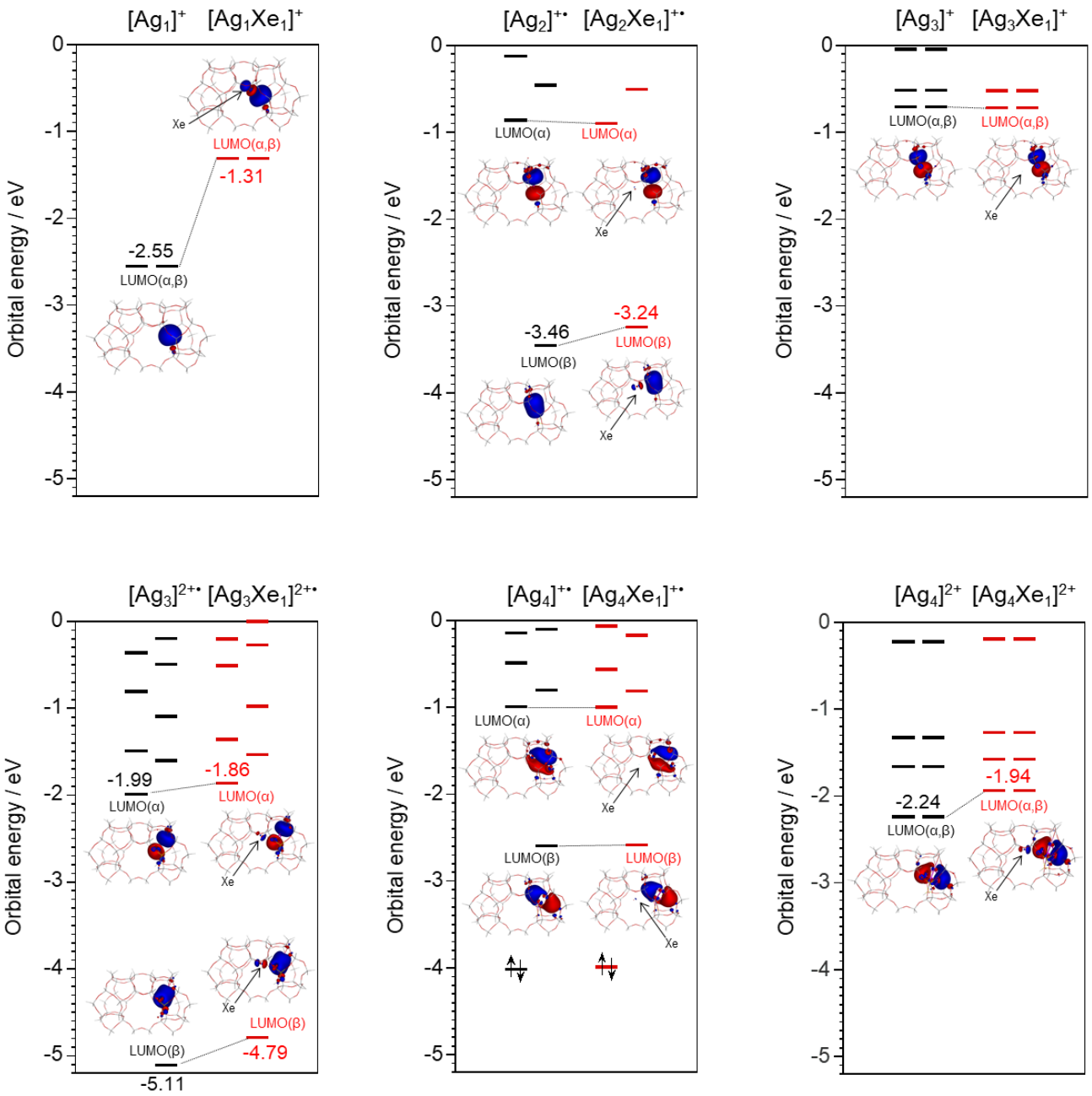

Figure S15. (A) Molecular orbital diagrams for the Ag_n^{m+} and $[Ag_nXe_1]^{m+}$ models. To focus on the Xe-5*p* →Ag-5*s* donation interactions, only the energy regions around the LUMO energy were shown in the figure. Both the LUMO energies for up-spin (*α*) and down-spin (*β*) were depicted separately. The schematic views of the respective LUMOs are available in **Figure S16**. For clarity, the geometries were represented as wireframe style. Legend: pink, Ag; light blue, Xe; gray, Si; yellow, Al; red, O; white, H.

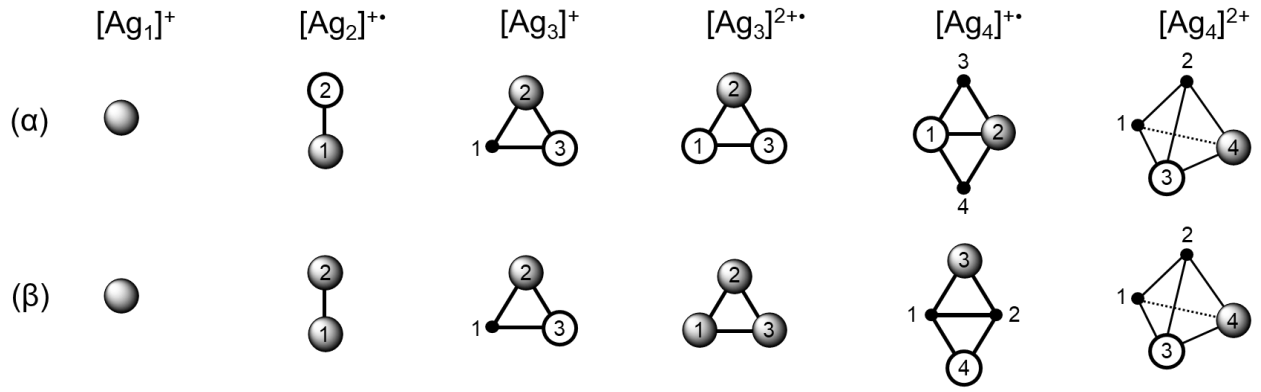

Figure S16. Schemes for the LUMOs for the $[Ag_n]^{m+}$ clusters. Both the up-spin (α) and down-spin (β) orbitals were depicted. All LUMOs are constructed via overlaps among the Ag-5*s* orbitals.

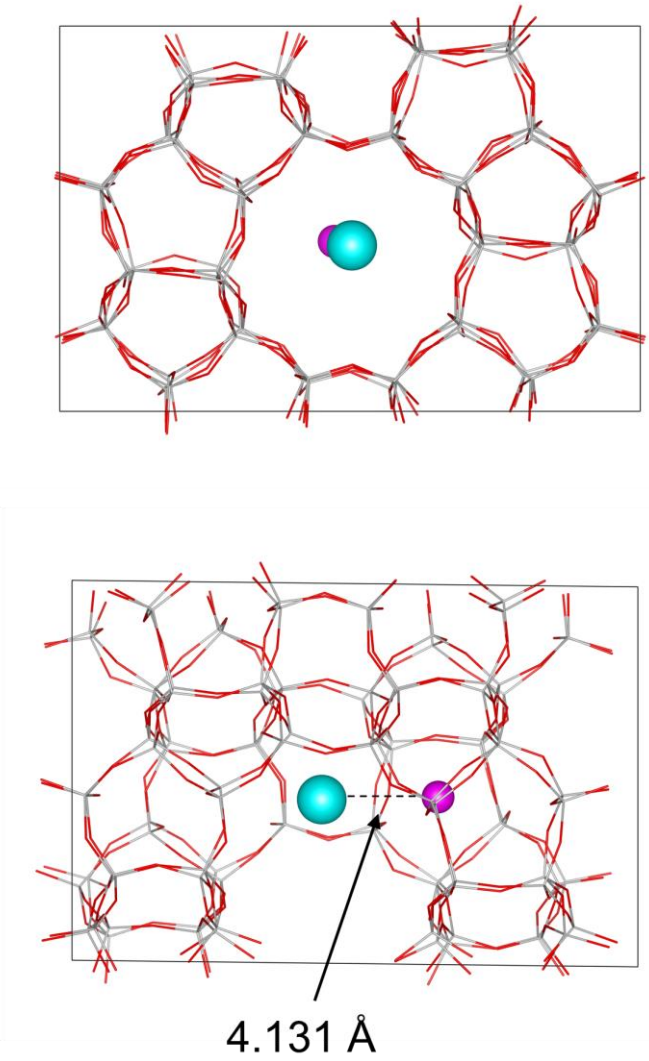

Figure S17. Optimized periodic DFT model representing the Xe adsorption at the Ag atom confined within the silicalite-1: (top) straight channel view; (bottom) sinusoidal channel view. The zeolite framework was represented as wireframe style for clarity. Legend: pink, Ag; light blue, Xe; gray, Si; red, O.

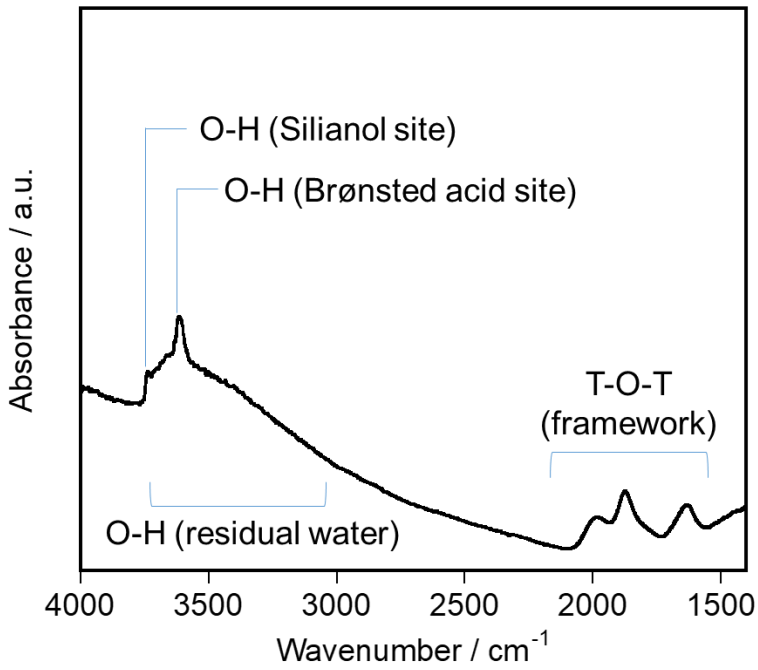

Figure S18. IR spectrum of the Ag/MFI sample after evacuation at 473 K.

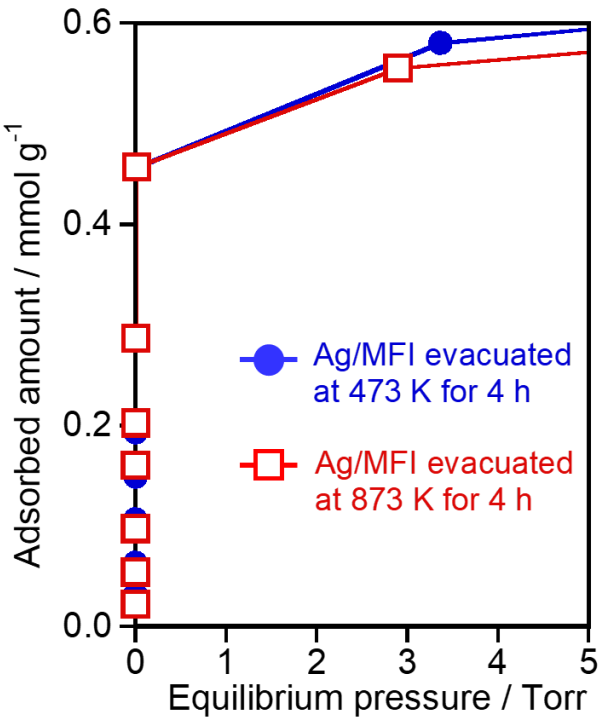

Figure S19. Comparison of the CO adsorption isotherms for the Ag/MFI sample pre-evacuated at 473 K and 873 K for 4 hours, which were measured at 298 K. Only the low-pressure region was depicted for clarity of the similarity of the CO-adsorption behavior of the single Ag(I) sites on the Ag/MFI sample preactivated at 473 K and 873 K.

3. Supporting References

1. Torigoe, H.; Mori, T.; Fujie, K.; Ohkubo, T.; Itadani, A.; Gotoh, K.; Ishida, H.; Yamashita, H.; Yumura, T.; Kobayashi, H., Direct information on structure and energetic features of Cu^{+}−Xe species formed in MFI-type zeolite at room temperature. *J. Phys. Chem. Lett.* **2010,** *1*, 2642−2650.

2. Yumura, T.; Nanba, T.; Torigoe, H.; Kuroda, Y.; Kobayashi, H., Behavior of Ag_3 clusters inside a nanometer-sized space of ZSM-5 zeolite. *Inorg. Chem.* **2011,** *50*, 6533−6542.

3. Yumura, T.; Oda, A.; Torigoe, H.; Itadani, A.; Kuroda, Y.; Wakasugi, T.; Kobayashi, H., Combined Experimental and Computational Approaches To Elucidate the Structures of Silver Clusters inside the ZSM-5 Cavity. *J. Phys. Chem. C* **2014,** *118*, 23874−23887.